Available online at www.sciencedirect.com
ScienceDirect
Trans. Nonferrous Met. Soc. China 35(2025) 194−206
Transactions of Nonferrous Metals Society of China
www.tnmsc.cn

As-cast $Ti_x(AlVCr)_{100-x}$ light-weight medium entropy alloys with high strength and uniform compressive plasticity

Ming-jie KAI[1], Yu-jie MA[2], Xiao-tian WANG[1], Liang CHENG[1], Jian-bo HU[3], Yao-yao HU[1], Tai-ran XU[1], Gui-jiang LI[1], Xiang-kang MENG[4], Zhen-hua CAO[1]

1. College of Materials Science and Engineering, Nanjing Tech University, Nanjing 210009, China;
2. School of Intelligent Manufacturing and Information, Jiangsu Shipping College, Nantong 226010, China;
3. Laboratory for Shock Wave and Detonation Physics, Institute of Fluid Physics, China Academy of Engineering Physics, Mianyang 621900, China;
4. National Laboratory of Solid State Microstructures, College of Engineering and Applied Sciences, Nanjing University, Nanjing 210093, China

Received 10 May 2023; accepted 20 December 2023

Abstract: The effect of Ti content on the microstructure and mechanical properties of as-cast light-weight $Ti_x(AlVCr)_{100-x}$ medium entropy alloys was studied by compressive tests, X-ray diffraction, scanning electron microscopy and transmission electron microscopy. The results suggest that yield strength increases and then decreases with the increment of Ti content. The $Ti_{60}(AlVCr)_{40}$ alloy has the best combination of high strength of 1204 MPa and uniform plastic strain of 70%, possessing a high specific yield strength of 255 MPa·cm^3/g. The enhancement of strength is mainly attributed to the synergic effects of solid-solution and coherent nano-precipitation strengthening, while dislocation motion such as dislocation pinning, entanglement and dislocation cells significantly increases the strain-hardening capacity.

Key words: TiAlVCr medium entropy alloy; solid solution strengthening; *b*2 precipitate; strain hardening behavior

1 Introduction

Developing novel light-weight structural metallic materials with high strength and sufficient plasticity has been a lasting endeavor for material researchers [1,2]. Over the past few decades, light-weight alloys with single dominant element have been widely reported, such as Al alloys, Mg alloys, and Ti-based alloys [3]. It becomes a new conundrum to further enhance the specific strength and plasticity simultaneously for the alloys based on one principal component. In recent years, the multi-component alloys, also called as medium entropy alloys (MEAs) or high entropy alloys (HEAs), containing multiple principal alloying elements have received considerable attention due to limitless compositional space, outstanding physical and mechanical properties, such as high strength, good fatigue, corrosion and oxidation resistance [4−6].

Similar to the conventional metallic alloys, the mechanical properties of MEAs also strongly depend on their microstructures and phase constituents. Generally, the single-phase face-centered-cubic (fcc) MEAs are ductile but soft, while the single-phase body-centered-cubic (bcc) MEAs exhibit a high strength but relatively poor

Corresponding author: Jian-bo HU, Tel: +86-816-2490709, E-mail: jianbo.hu@caep.cn;
Zhen-hua CAO, Tel: 86-25-83587270, E-mail: zhenhuacao@njtech.edu.cn
https://doi.org/10.1016/S1003-6326(24)66674-4

plasticity [7]. Several strengthening approaches have been implemented to improve the strength and strain hardening capability of single-phase MEAs [8]. For example, numerous light-weight MEAs (LW-MEAs) with single bcc phase solid-solution structure have been developed, such as $Ti_{67-x}Nb_{25}Zr_8Cr_x$, $(Ti_{67}Nb_{16}Zr_{17})_{100-x}Al_x$, $Ti_{60}Al_x$-$(VCrNb)_{40-x}$, $Ti_x(AlCrNb)_{100-x}$ and $Ti_x(AlCr$-$VNb)_{100-x}$ [9,10]. The high mechanical properties of these alloys are attributed to the single solid-solution strengthening effect caused by the severe lattice distortion. In addition to the intrinsic solid-solution strengthening of MEAs, nanoprecipitate-strengthening MEAs also can carry a high strength while maintaining a decent plasticity. For instance, YANG et al [11] have prepared the single-phase fcc $(FeCoNi)_{86}Al_7Ti_7$ HEA with a high-volume fraction nanoprecipitates, where superior yield strength over ~1 GPa and no plasticity loss were obtained due to the uniform distribution of $L1_2$ nanoprecipitates within the grain. In contrast, SHIRATORI et al [12] used the ordered *b*2 precipitate phases to strengthen the AlCoCrFeNi HEA, where the compressive yield strength was increased to ~1.3 GPa, but the plasticity was limited to ~5.6%. The reason for the reduced plasticity is the weave-like microstructure induced by the spinodal decomposition of bcc phases and sub-micron *b*2 precipitation. Therefore, the volume fraction, size and distribution of the precipitates are crucial to improve strength while reduce the loss of plasticity.

Based on these considerations, Al, Ti, V and Cr which have relatively low density were chosen to develop strong LW-MEAs. On account of similar crystal structure of Ti, V and Cr, they provide bcc solid-solution phase. Meanwhile, Al could further enhance the stability of bcc solid-solution phase as bcc stabilizing element. On the other hand, Ti has the largest radius size (~145 pm) compared to other elements, so the solid-solution strengthening effect can be regulated by adjusting the Ti content. Moreover, Ti has significantly negative mixing enthalpy with Al and Cr, and nanoprecipitates can be obtained by controlling the content of Ti. Thus, we developed a series of Ti-rich light-weight MEAs in the composition of $Ti_x(AlVCr)_{100-x}$. In addition, the strain hardening behavior and corresponding deformation mechanism were investigated in detail.

2 Experimental

2.1 Materials design and preparation

According to the knowledge of thermodynamics and the Hume Rothery rule for multi-component alloys, the enthalpy of mixing (ΔH_{mix}), atomic size difference ($\Delta\delta_r$), thermodynamic parameter (Ω), electronegativity difference ($\Delta\chi$) and valence electron concentration (VEC) are proposed to evaluate the phase formation and structural stability [13−15]. Particularly, the near zero values of the absolute ΔH_{mix}, the small $\Delta\delta_r$ and $\Delta\chi$, and large values of Ω have been widely believed to effectively favor the formation of the stable solid-solutions rather than that of complex intermetallic compounds. It was determined that the criteria for forming high-entropy stabilized solid-solution phases region is $-20\ kJ/mol \le \Delta H_{mix} \le 5\ kJ/mol$, $\Delta\delta_r \le 6.6\%$, $\Omega \ge 1.1$ and $\Delta\chi \le 17.5\%$. Obviously, the calculated values in Table 1 indicated that the parameters of these LW-MEAs meet the criteria for stable solid-solution formation. In addition, the VEC was found to be the physical parameter to control the phase stability for fcc or bcc solid solutions. The systems with lower VEC values than 6.87 tend to form bcc phases and those with higher values larger than 8 tend to form fcc phases. The calculated VEC values of these alloys are all smaller than 6.87, and it could be concluded that all as-cast LW-MEAs are located in the bcc solid solution zone.

Table 1 Mixing enthalpy (ΔH_{mix}), difference of atomic radius (δ_r), thermodynamic parameter (Ω), electro-negativity difference ($\Delta\chi$) and valence electron concentration (VEC) of LW-MEAs

Alloy composition/at.%	ΔH_{mix}/ (kJ·mol^{-1})	δ_r/%	Ω	$\Delta\chi$/%	VEC
$Ti_{40}(AlVCr)_{60}$	−16.96	5.06	1.19	5.0	4.40
$Ti_{50}(AlVCr)_{50}$	−16.11	4.86	1.18	5.4	4.33
$Ti_{60}(AlVCr)_{40}$	−14.47	4.54	1.19	5.8	4.26
$Ti_{70}(AlVCr)_{30}$	−12.04	4.09	1.22	6.1	4.20
$Ti_{80}(AlVCr)_{20}$	−8.81	3.46	1.29	6.4	4.13

Five kinds of $Ti_x(AlVCr)_{100-x}$ (x=40, 50, 60, 70 and 80, at.%) LW-MEAs (denoted as Ti40, Ti50, Ti60, Ti70 and Ti80 MEAs) were fabricated by vacuum induction-melting process (Fig. 1), using

the mixtures of Ti, Al, V, and Cr raw materials with high purity (>99.95 wt.%). Prior to melting, the furnace was first evacuated to 6×10^{-3} Pa and then backfilled with high-purity Ar_2 and evacuated three times to dilute the residual air inside the chamber, finally it was filled back to a vacuum degree lower than 3×10^{-3} Pa. Approximately 300 g of master metals were weighed and poured into a cylindrical copper crucible with the length of 50 mm and inner diameter of 35 mm. The alloy ingots were flipped and remelted at least five times to ensure thorough mixing and chemical homogeneity. The density of each ingot alloy was measured by the Archimedes method. The nominal and actual composition of as-cast $Ti_x(AlVCr)_{100-x}$ LW-MEAs are given in Table 2. The design components were nearly the same as the actual values, and there was no obvious Al evaporation during the melting process.

2.2 Microstructural characterization

Phase analysis was conducted by an X-ray diffraction (XRD, SmartLab TM 9KW) with Cu K_α radiation in a 2θ range from 30° to 80° at a scanning rate of 5 (°)/min. Microstructures were characterized with TESCAN S8000 GMH scanning electron microscope (SEM) equipped with an energy dispersive (EDS) detector, operating in the back-scatter electron (BSE) mode at an accelerating voltage of 20 kV and a transition electron microscope (TEM, JEM-2010UHR). The SEM specimens for microstructural observations were prepared by mechanically grinding with 1000−6000 grit silicon-carbide (SiC) abrasive papers, followed by polishing with the optical microscopy (OM) suspension. The polished samples were etched with the etchant consisting of 5 vol.% HF, 8 vol.% HNO_3, and 87 vol.% H_2O.

2.3 Mechanical tests

The compressive tests were conducted using electronic universal testing machine (ETM205D) with cylindrical specimens (d3 mm × 6 mm) under

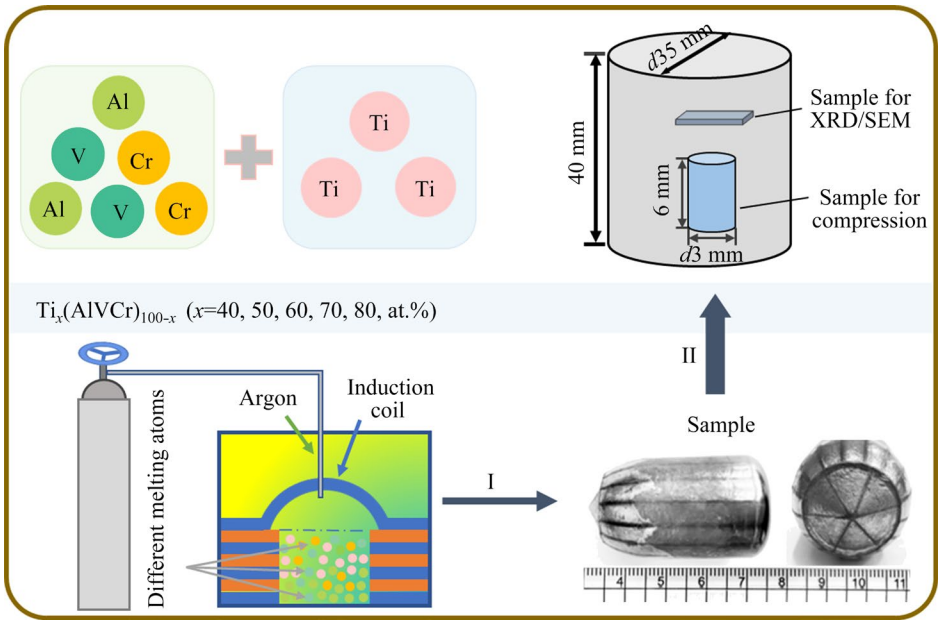

Fig. 1 Schematic diagram of preparation process for LW-MEAs

Table 2 Nominal and actual composition of as-cast $Ti_x(AlVCr)_{100-x}$ LW-MEAs

Alloy	Nominal composition/at.%				Actual composition/at.%			
	Ti	Al	V	Cr	Ti	Al	V	Cr
Ti40	40.00	20.00	20.00	20.00	39.24	19.88	21.39	19.49
Ti50	50.00	16.67	16.67	16.67	49.49	16.07	17.82	16.62
Ti60	60.00	13.33	13.33	13.33	59.95	12.96	13.54	13.55
Ti70	70.00	10.00	10.00	10.00	69.51	9.83	10.74	9.92
Ti80	80.00	6.67	6.67	6.67	79.77	6.13	7.20	6.90

a constant engineering strain rate of 1×10^{-3} s^{-1} at room temperature. The dog-bone shaped tensile specimens with a gauge size (20 mm × 8 mm × 1.5 mm) were tested with the electronic universal testing machine (INSTRON 5985). Before testing, the specimen surfaces were mechanically polished using 2000 grit SiC abrasive papers. For the accuracy of experimental results, all the tests were repeated at least three times. In addition, to analyze the deformation mechanism, some compressive tests were interrupted at the selected strain levels to observe deformation microstructure.

3 Results and discussion

3.1 Microstructure and phase constitution

As shown in Figs. 2(a, b), the XRD patterns reveal that the as-cast $Ti_x(AlVCr)_{100-x}$ MEAs possess single disordered bcc solid solution structure. From the enlarged XRD pattern in the range from 39° to 42°, the diffraction peaks shift towards a lower-angle with Ti content increment, indicating the increase of the lattice parameter and severe lattice distortion. Furthermore, the low-angle superlattice diffraction peak at 2θ=31.2° attributed to the (100) plane of *b*2 ordered-phase appears when the Ti content reaches 60 at.%. The inset image in Fig. 2(b) further indicates the presence of *b*2 phase. The back-scattering electron microscope (BSE) images of the as-cast alloys shown in Figs. 2(c−e) display a typical coarse-grained structure. The average grain size of these investigated MEAs determined by linear interception method is (500±50) μm.

The bright-field (BF) TEM image of the as-cast Ti60 MEA is shown in Fig. 3(a), which clearly presents single-phase bcc solid solution structure. Magnified BF TEM image in Fig. 3(b) further reveals a decent amount of *b*2 nano-precipitates are in a spherical shape dispersed coherently in the bcc matrix. Figure 3(c) shows the diameter distributions of *b*2 nano-precipitates. The average size is approximately 24 nm. The corresponding selected area electron diffraction (SAED) pattern along with the [111] zone axis further reveals that the matrix is a disordered bcc phase (Fig. 3(d)), while the SAED pattern along with [001] zone axis indicates that the precipitate has an ordered *b*2 structure (Fig. 3(e)). This is agreed with the result of XRD. The BF TEM micrograph of the as-cast Ti80 MEA shown in Fig. 3(f) also shows the single-phase bcc solid solution structure. Several nano-precipitates with an average thickness of 71 nm distribute uniformly in

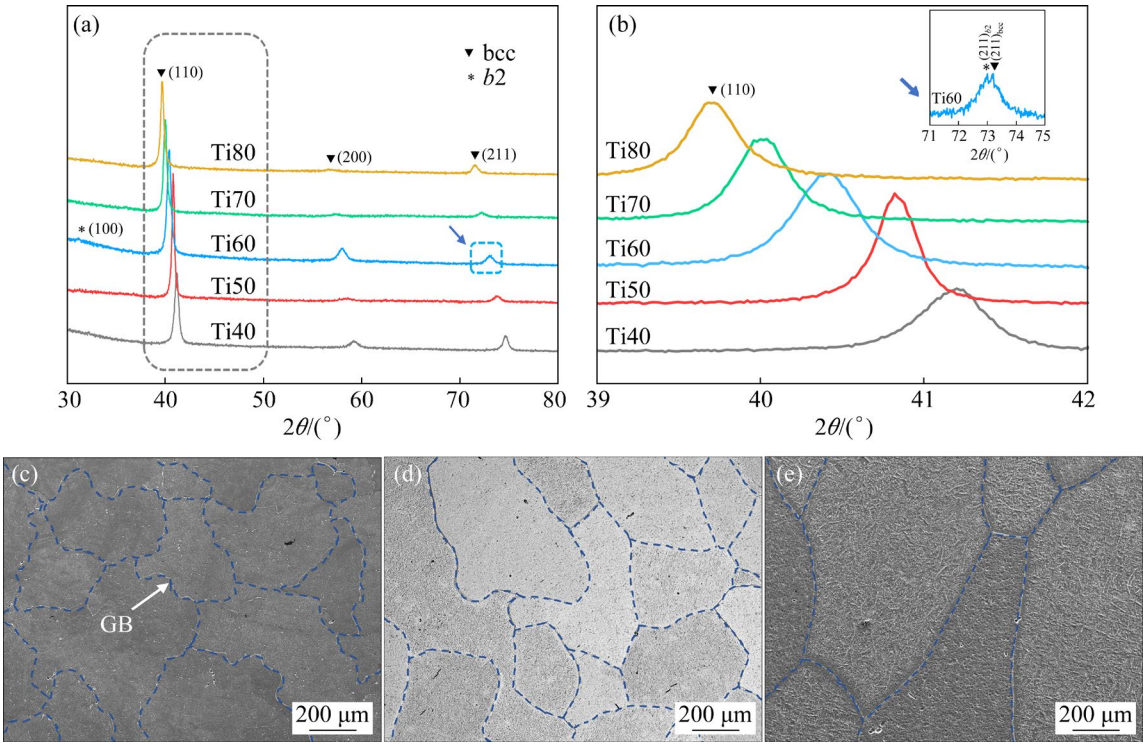

Fig. 2 XRD patterns of as-cast LW-MEAs (a), enlargement of $(110)_{bcc}$ peak (b) and BSE-SEM images of as-cast Ti40 (c), Ti60 (d) and Ti80 (e) MEAs

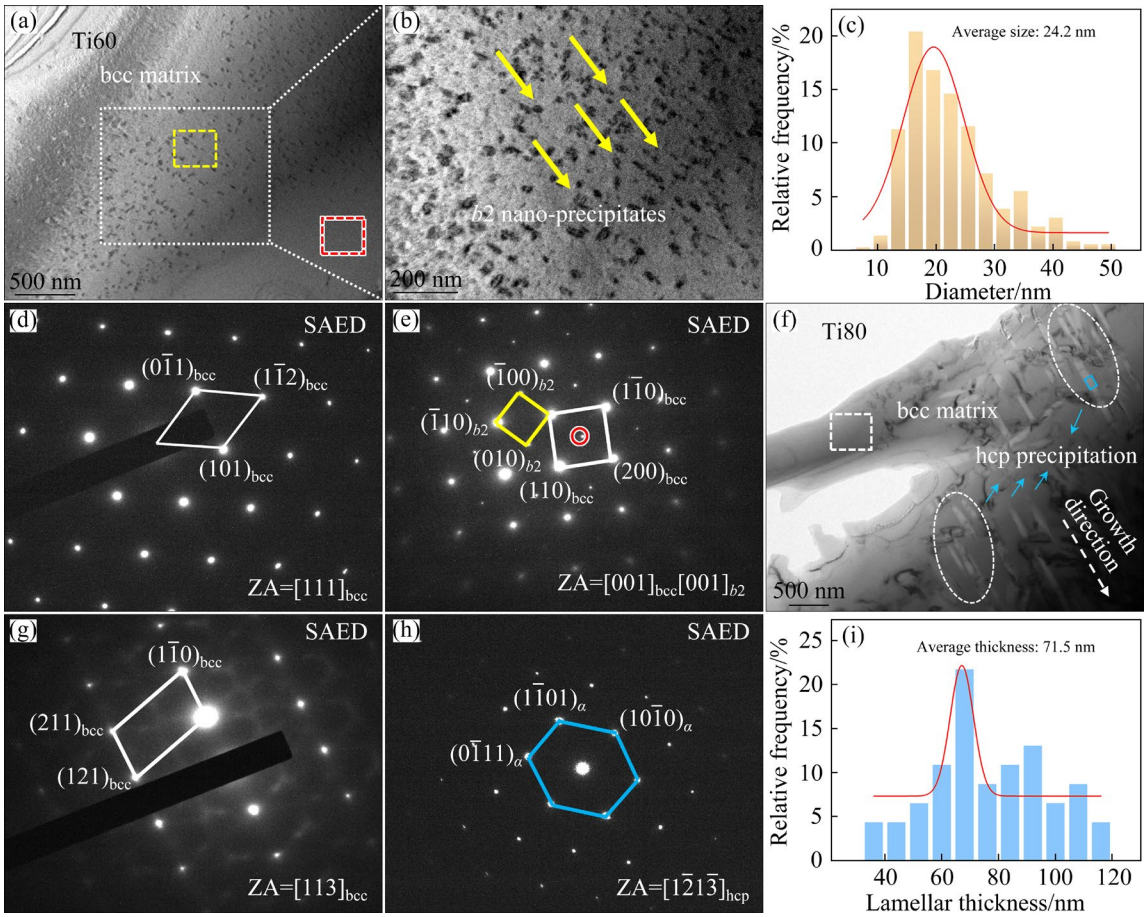

Fig. 3 TEM characterization and corresponding SAED patterns of Ti60 and Ti80 MEAs: (a) BF TEM image of bcc/*b*2 region; (b) Magnified BF TEM image showing central region of bcc/*b*2 phase; (c) Size distribution of *b*2 precipitates; (d, e) SAED patterns of bcc phases and bcc/b2 phases; (f) BF TEM image showing hcp precipitates in bcc matrix; (g, h) SAED patterns of bcc phases and hcp phases; (i) Thickness distribution of hcp precipitates

the matrix. The SAED pattern obtained for the matrix along the [113] zone axis reveals a disordered bcc structure (Fig. 3(g)), while the SAED pattern in Fig. 3(h) obtained for the fine lamellar phase indicates that the nano-precipitates have hexagonal centered cubic (hcp) crystalline structure.

3.2 Mechanical properties

The compressive engineering stress−strain curves of the as-cast LW-MEAs at room temperature are shown in Fig. 4(a). Among the investigated alloys, the Ti40 and Ti50 MEAs exhibit the poor plastic strain of 6.1% and 6.8%, respectively, and the relatively low yield strength of 634.6 and 883.6 MPa, respectively. The Ti40 and Ti50 alloys containing high Al content possess a higher negative ΔH_{mix} value (<−16.11 kJ/mol) compared to the other three MEAs, which are more conducive to the formation of highly ordered crystal structures, leading to the inferior plasticity at room temperature. For example, AlTiVNb [16], AlTiVCr [17], AlTiVNbZr [18] and AlTiVCrNb [19] alloys exhibit similar brittle fracture behavior (<1%) caused by highly ordered structures. As Ti content increases to 60 at.%, the degree of order to disorder transition for the alloy is lowered, and an obvious brittle-to-ductile fracture transition behavior occurs. The yield strength and plastic strain both dramatically increase. Also, the as-cast Ti60 MEA with low density (4.71 g/cm^3) displays an ultra-high yield strength of 1204 MPa and superior compressive plasticity over 70%. It is noted that the alloy still shows a relatively low tensile elongation below 1%. With increment of Ti content from 60 to 80 at.%, the strengthening effects are gradually reduced. Compared with the Ti60 MEA, the yield strength of Ti70 and Ti80 MEAs decreases to 1002 and 784 MPa, respectively, whereas these Ti-rich MEAs display excellent compressive plasticity.

The yield strength and specific yield strength of the LW-MEAs are displayed in Fig. 4(b). As the Ti content increases from 40 to 60 at.%, the specific yield strength increases rapidly from ~132 to 255, and then decreases to 170 MPa·cm^3/g at the Ti content of 80 at.%. The variation trend of yield strength is consistent with the specific yield strength.

Figure 5 shows the specific yield strength and compressive plasticity of the Ti60 LW-MEA compared with the most reported Ti-rich M/HEAs and part of previously reported LW-M/HEAs [10,20,21]. Obviously, the present as-cast Ti-rich LW-MEAs exhibit a higher specific yield strength comparable to the reported LW-H/MEAs, together with pretty good compressive plasticity. Overall, the as-cast Ti60 MEA exhibits the best combination of yield strength, plasticity and specific yield strength.

Figure 6 displays the true stress−strain and strain-hardening rate ($d\sigma/d\varepsilon$) curves of the as-cast Ti60 MEA. Interestingly, the deformation processes of the alloy can be classified into three distinctive stages, which are elastic deformation, strain-hardening and strain-softening stages. It is found that the strain-hardening rate shows a fairly high level at the beginning of the elastic deformation, while it drops drastically with increasing the strain, and then maintains a relatively high level of 1500−2000 MPa. However, the strain hardening capacity of the alloy exhibits a gradually decreasing trend with increasing the strain.

3.3 Evolution of deformation substructure

The strain hardening behavior is essentially related to the dislocation substructure evolution upon plastic deformation. To reveal the underlying deformation behavior responsible for the super strain-hardening capacity of the cast Ti60 MEA,

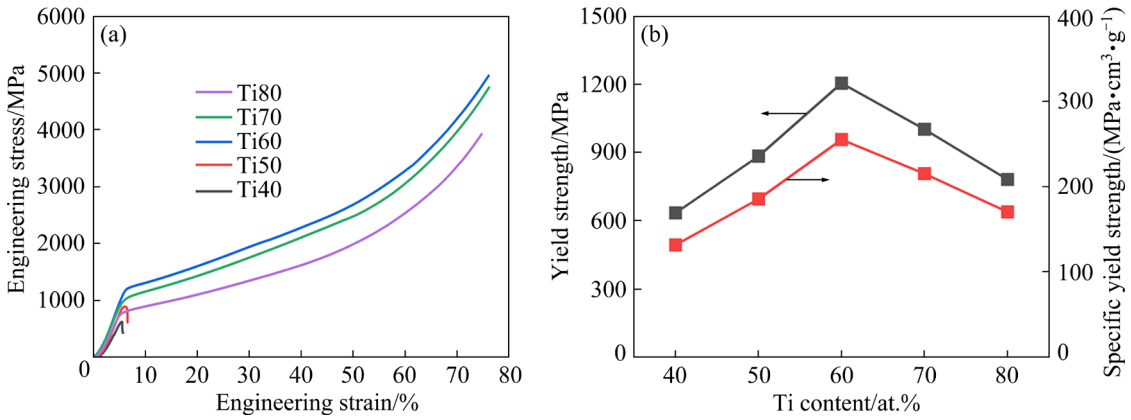

Fig. 4 Compressive engineering stress−strain curve of as-cast LW-MEAs (a) and variation of yield strength and specific yield strength with Ti content (b)

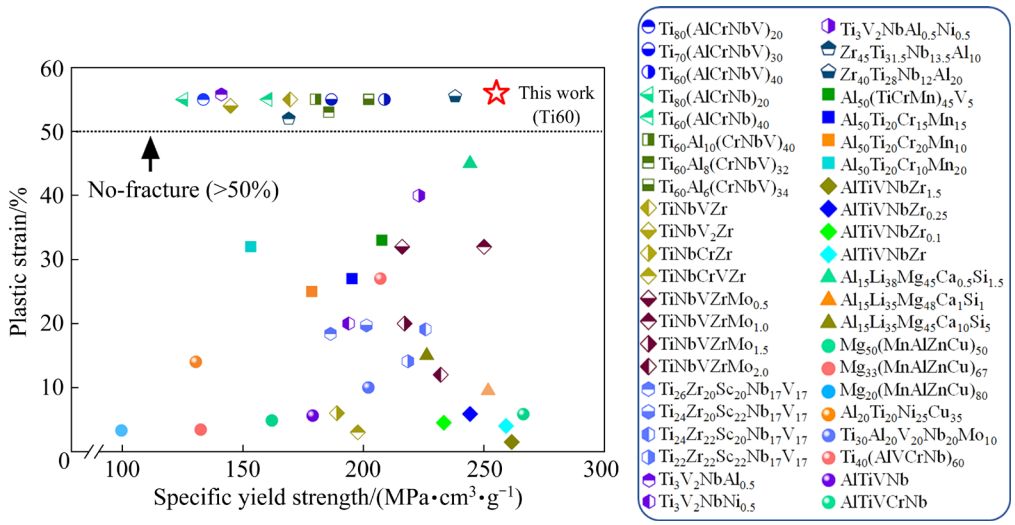

Fig. 5 Exceptional combination of compressive strain and specific yield strength comparison to various reported LW-MEAs [10,20,22,23]

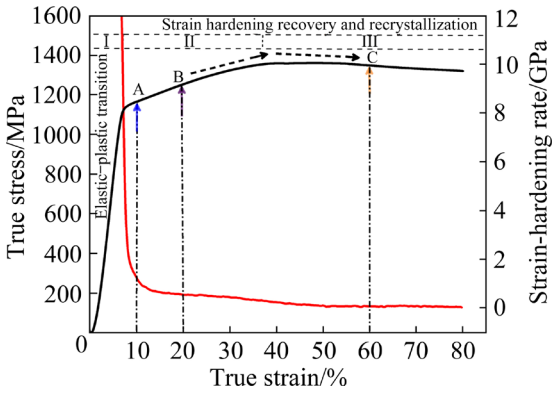

Fig. 6 True stress−strain and stain-hardening rate curves of Ti60 LW-MEA

microstructure evolution is characterized by TEM for the sample deformed at the plastic strain of 10%, 20% and 60%. After the relatively low compressive strain level of 10% shown in Figs. 7(a, b), the evident dislocation movements involving coplanar dislocation arrays and surface slip bands resulting from dislocation planar slip are observed. In addition, the local dislocation pinning points (indicated by red arrows) and dislocation loops appear in the deformed matrix. Generally, the products of dislocation loops are caused by double cross-slip of screw dislocations [24,25]. Such dislocation substructures indicate that the early plastic deformation stage is developed by planar

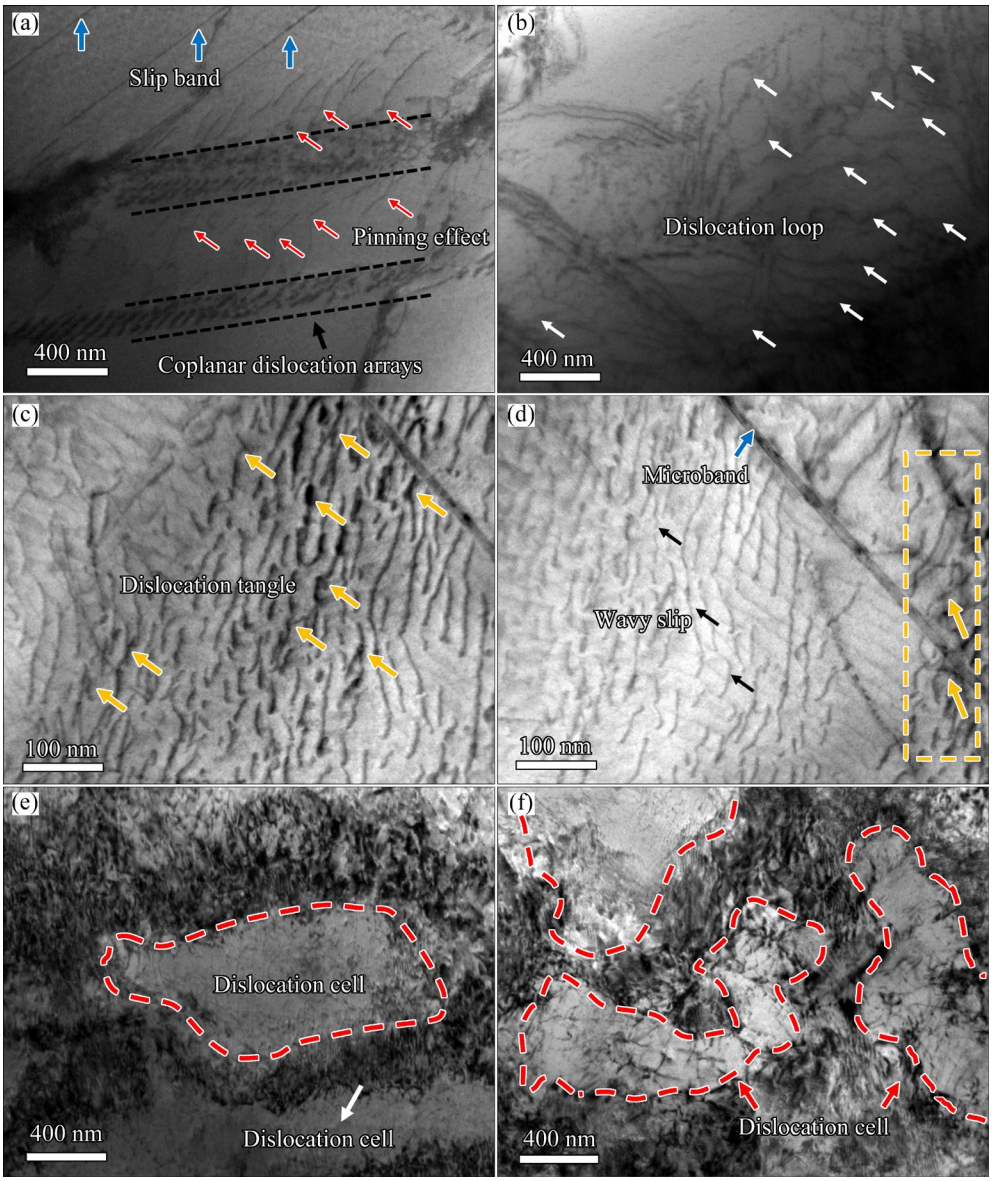

Fig. 7 Typical microstructures of Ti60 MEA deformed at different interrupted strains: (a, b) 10% strain, showing different dislocation activities; (c, d) 20% strain, showing tangled dislocation and significant increase in dislocation density; (e, f) 60% strain

and wavy multiple slip. As the strain level increases to 20%, a significant increase in the dislocation density is observed. Meanwhile, the interaction between dislocations gets stronger, dislocation slips become difficult, and a large amount of highly curved dislocations are entangled, induced by the promotion of cross slip, as shown in Figs. 7(c, d). With increase in strain to a higher level of 60%, the disordered high-density dislocations gradually intertwin to form dense dislocation walls (DDWs), further constructing sub-grains.

In addition, the plastic strain magnitudes at the different regions are locally nonuniform after highly large deformation. In the moderate deformation area, as shown in Figs. 8(a, b), the initial high-angle grain boundaries and coarse-grained regions with less dislocation accumulation are still observed, unable to transform into a sub-grain. In contrast, the severe deformed regions with high density tangled-dislocations exist with typical dislocation wall structures accompanied by cellular structures with a space of 300−500 nm. The dislocation density inside the dislocation cell surrounded by the dislocation walls is very low. Additionally, the severe deformed regions undergo a dynamic recovery and recrystallize process with dislocation transforming into sub-grains and equiaxed fine-grains, as shown in Figs. 8(c, d).

3.4 Plastic deformation mechanism

In the as-cast MEAs, the variation of Ti content significant changes the mechanical properties. As the Ti content is below 50 at.%, the MEAs exhibit a typical brittle fracture behavior. In contrast, as the Ti content increases from 60 to 80 at.%, the MEAs achieve the excellent balance between strength and plasticity. Most intriguingly, the as-cast Ti60 sample obtains the best combination of strength and plasticity. The solid-solution strengthening and coherent nano-precipitation strengthening are responsible for the outstanding mechanical properties.

3.4.1 Solid solution strengthening (SSS)

In traditional binary alloys, the SSS effect is attributed to the interaction of the solute atoms and moving dislocations, as described by Labusch's and Fleischer's models. In terms of the H/MEAs, also called the multi-component alloys, the SSS effect induced by lattice distortion is distinctly different from conventional binary alloys, since it is difficult

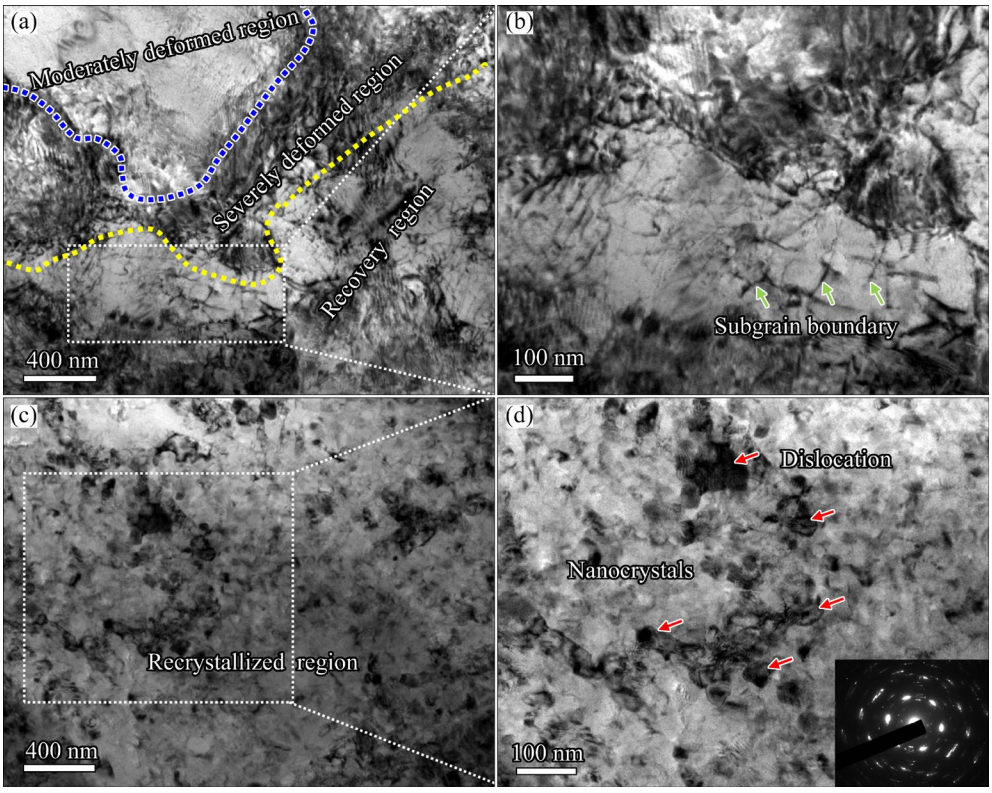

Fig. 8 TEM images of Ti60 MEA after 60% strain: (a) BF TEM image showing locally nonuniform plastic strain at different regions after highly large deformation; (b) Magnified BF TEM image showing distinct recovery region; (c) BF TEM image showing recrystallization region; (d) Magnified BF TEM image further indicating presence of nanocrystals

to term “solute” or “solvent”. The severe lattice distortion originating from large atomic radius difference and elastic misfit, is generally believed to generate a repulsive or attractive interaction with dislocations [26−28]. Therefore, the Fleischer’s and Labusch’s models are not appropriate for the multi-component systems. Recently, TODA-CARABALLO et al [29] have proposed a modified model based on Labusch’ approach to calculate the interatomic spacing in M/HEAs, which well determines the SSS contribution ($\Delta\sigma_{ss}$) on yield strength:

$$\Delta\sigma_{ss}=3Z\mu\left(\sum_i c_i\left(\eta_i'+\alpha^2\delta_i'^2\right)\right)^{2/3} \quad (1)$$

$$\eta_i'=\frac{9}{8}\sum c_j\eta_{ij} \quad (2)$$

$$\delta_i'=\frac{9}{8}\sum c_j\delta_{ij} \quad (3)$$

where Z is a fitting constant, μ is the shear modulus of the solvent elements, η_i' and δ_i' are the average modulus misfit and size misfit, respectively, and α describes the difference in interaction forces between the screw and edge type dislocations and the foreign atoms. c_j is the molar ratio of element j; δ_{ij} and η_{ij} are the relative atomic size difference and modulus difference between element i and element j, respectively. By using these given equations, the calculated η_{Ti}' and δ_{Ti}' values in Ti60 MEA are 0.0547 and 0.0438, respectively, much larger than those of Ti70 and Ti80 MEAs. Obviously, effect of Ti atoms on the dislocation force in Ti60 MEA produces a far severe distortion effect, consistent with our experiment data. Moreover, the result also shows that the magnitudes of modulus distortions are likely to be stronger obstacles for dislocation movements in this alloy than the lattice distortions. Indeed, the arrangement of atoms in M/HEAs may not be an ideal disordered state due to the complex interaction between the constituent elements and the diversity of atomic sizes [30,31]. As a result, chemical short-range orders (CSROs) may exist in the M/HEAs, and the SSS model does not take into account the intervene of CSROs, which affects the interaction of the solute atoms and moving dislocations, further leading to the alteration of dislocation slip pathway [32,33].

In this model, the predicted yield strength ($\sigma_{\mathrm{y}}^{\mathrm{cal}}$) of MEAs is obtained:

$$\sigma_{\mathrm{y}}^{\mathrm{cal}}=\Delta\sigma_{SS}+\sigma_{\mathrm{mix}} \quad (4)$$

$$\Delta\sigma_{\mathrm{mix}}=\sum_{i=1}^{n}\sigma_{\mathrm{y},i}X_i \quad (5)$$

where σ_{mix} is the yield stress of the nominal solvent matrix, $\sigma_{\mathrm{y},i}$ and X_i are the yield strength and content of each constituent element. Eventually, by using these given equations, the calculated $\Delta\sigma_{SS}$ and $\Delta\sigma_{\mathrm{mix}}$ values in Ti60 MEA are determined to be 743 and 207 MPa (Fig. 9), respectively. By comparing the experimentally measured yield strength and the predicted yield strength, the latter is lower than the former. Therefore, there should be other strengthening mechanism responsible for the high yield strength of the samples.

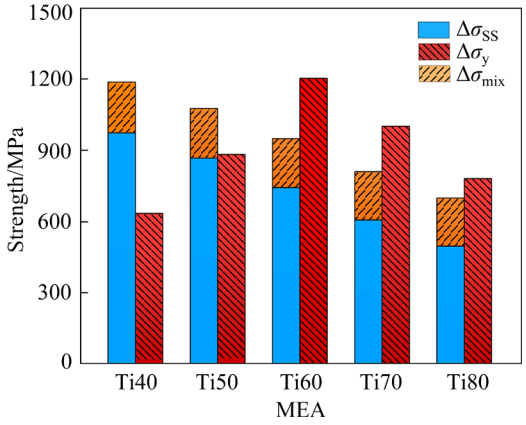

Fig. 9 Calculated $\Delta\sigma_{SS}$, σ_{mix} and $\Delta\sigma_{\mathrm{y}}$ values of investigated LW-MEAs

3.4.2 Precipitation strengthening

Based on the interaction between mobile dislocations and precipitates, the mechanism for precipitation strengthening can be divided into two categories: Orowan bowing and particle shearing. Generally, the shearing mechanism occurs when the precipitates are coherent or small, while the Orowan mechanism dominates when the precipitates are large or incoherent with the matrix [34−36]. For the Ti60 sample, the lattice misfit (δ_{a}) between bcc and $b2$ phases can be calculated:

$$\delta_{\mathrm{a}}=2(a_{b2}-a_{\mathrm{bcc}})/(a_{b2}+a_{\mathrm{bcc}}) \quad (6)$$

where a_{bcc} and a_{b2} represent the lattice constants of bcc and $b2$ phases, respectively, and the value of δ_{a} is determined to be 0.21%, which indicates that the interface between the two phases is fully coherent. Thus, the shearing mechanism dominates the coherent precipitation strengthening in the current

MEA. The coherency strengthening ($\Delta\sigma_{cs}$) can be evaluated based on the equation [36]:

$$\Delta\sigma_{cs}=M\alpha_{\varepsilon}\left(G\varepsilon_{c}\right)^{\frac{3}{2}}\left(\frac{rf}{0.5Gb}\right)^{1/2} \quad (7)$$

where M (=2.73) is the Taylor Factor for the bcc structure, α_{ε} (=2.6) is a constant, G is the shear modulus of matrix, ε_{c} (=$2\delta_{a}/3$) is the constrained lattice misfit, b (=$\sqrt{3}a_{bcc}/2$) is the magnitude of Burgers vector of the matrix, r is the average particle size and f is the volume fraction of the precipitates. Based on the above equations and parameters, the coherent precipitation strengthening value for the as-cast alloy sample is calculated to be ~206 MPa. Thus, the coherency strain field formed around the precipitates can effectively hinder the dislocation motion, thereby increasing the strength effect. Meanwhile, *b*2 nano-precipitates distributed in the bcc matrix can produce the shear-modulus mismatch between the precipitate and matrix. Numerous misfit dislocation existing at the *b*2/bcc interface occurs to accommodate the misfit [21,37]. As a result, there is a strong stress field around the interfacial misfit dislocations, which can bring about a stronger elastic interaction between the *b*2 and bcc phases during the plastic deformation, thus leading to the enhancement for the strain-hardening capability. In addition, the hard ordered nano-precipitated phases are generally identified as primary strengthening agents for metallic materials since they are more effective in obstructing dislocation migration and rendering the dislocation accumulation and tangle [38].

3.5 Strain hardening behavior

To better explain this strain hardening behavior, a schematic diagram is used to show the dislocation substructure evolution in details (Fig. 10). At the initial elastic−plastic deformation transition of Stage I, the density of movable dislocations maintains at a relatively low level, and the rate of dislocation accumulation is negligible. Thus, the dynamic recovery becomes prominent, resulting in a striking decrease of strain-hardening rate for the alloy.

As the strain increases into Stage II, due to the occurrence of a fast dislocation nucleation and massive multiplication, the density of movable dislocations increases to a certain degree [39]. Moreover, the emergence of multiple dislocation activities, especially the dislocation pinning and entanglement, not only strengthens the alloy but also enhances the strain hardening capacity. Thus, the strain-hardening rate in Stage II shows an upward trend (Fig. 6). As the strain increases into Stage III, the dislocation densities further increase, and dislocation cell and DDWs structures dominate the deformed microstructures. The formation of the DDWs is generally attributed to the increase of local strain concentration in some deformation areas, which is beneficial to enhancing the strength of the alloy [40,41]. Additionally, the dislocation wall is a typical short-range obstacle to dislocations slip, which can act as the grain boundary of the substructure. During the plastic deformation process, the DDWs can effectively accommodate a number of geometrically necessary dislocations, resulting in sustainable strain-hardening rates and stable plastic deformation ability [42]. Thus, the strain-hardening rate in Stage III (Fig. 6) still maintains at a high level.

However, the severe accumulative deformation process can store continuously accumulating deformation energy in the samples. Due to the intrinsic delay diffusion effect of M/HEAs [43,44], it is difficult for the local heating of deformation to diffuse and make some grains dynamically recrystallize, leading to the dislocation cells and

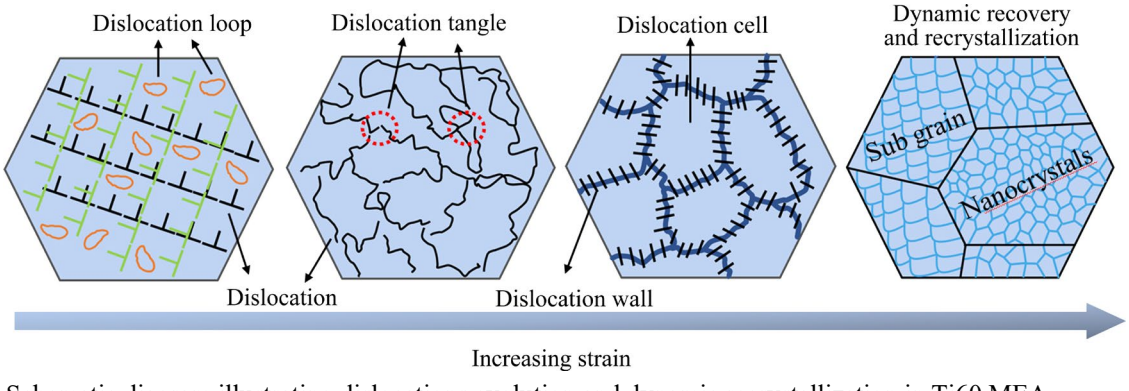

Fig. 10 Schematic diagram illustrating dislocations evolution and dynamic recrystallization in Ti60 MEA

sub-grains being partially replaced by new equiaxed fine-grains. At the same time, the dislocation density decreases significantly, and the stored strain energy in the crystal is released and tends to be stable, as shown in Figs. 8(c, d). Thus, the strain-hardening rate in Stage III (Fig. 6) shows a slow decreasing trend due to dynamic recovery and recrystallize process. Similar phenomenon was observed in bulk coarse-grained pure metal and HEAs by means of quasistatic and dynamic compression tests at room temperature [45−47]. A significant grain refinement occurs after heavily deformed compression process, whose magnitude increases with increasing both strain and strain rate. The grain size reduction is caused by partial recrystallization due to the driving force of activation thermal energy and self-diffusion for grain boundary migration.

4 Conclusions

(1) With the increment of Ti content, the mechanical properties of $Ti_x(AlVCr)_{100-x}$ LW-MEAs are significantly improved. Among these investigated alloys, the best comprehensive performance is achieved in as-cast $Ti_{60}(AlVCr)_{40}$ sample with bcc/*b*2 coherent microstructure.

(2) Compared to Ti40 samples, the yield strength of Ti60 sample is increased by 50%, which is considered as an optimal combination of solid solution and coherent nano-precipitation strengthening effects.

(3) The dislocation-dominated deformation mechanism involving dislocation cells and dislocation pining in the Ti60 sample serves to enhance the strain-hardening capacity, resulting in the dramatic improvement of plasticity from 6.1% to an extremely high value of >70%, which shows great potential application of M/HEAs as novel high-performance light-weight structural materials.

CRediT authorship contribution statement

Ming-jie KAI: Conceptualization, Methodology, Validation, Formal analysis, Date curation, Writing − Original draft, Visualization; **Yu-jie MA:** Investigation, Methodology, Formal analysis; **Xiao-tian WANG:** Methodology, Validation, Formal analysis; **Liang CHENG:** Data curation, Formal analysis; **Jian-bo HU:** Investigation, Supervision; **Yao-yao HU:** Formal analysis, Visualization; **Tai-ran XU:** Investigation, Visualization; **Gui-jiang LI:** Visualization, Formal analysis; **Xiang-kang MENG:** Formal analysis, Funding acquisition; **Zhen-hua CAO:** Resources, Writing − Review & editing, Supervision, Funding acquisition, Project administration.

Declaration of competing interest

The authors declare that they have no known competing financial interests or personal relationships that could have appeared to influence the work reported in this paper.

Acknowledgments

This work was jointly supported by the National Natural Science Foundation of China (Nos. 52071176, 12072331, 51771090, 51671103), and the Priority Academic Program Development (PAPD) of Jiangsu Higher Education Institutions, China.

References

[1] KAI M J, MA Y J, ZHAI G Y, MA H, LI G J, HU J B, WANG H, CAO Z H. Simultaneous strength−plasticity enhancement of dual-phase light-weight medium entropy alloy [J]. Journal of Alloys and Compounds, 2022, 923: 166406.

[2] DU Hui, CAI Jia-hong, WANG Ya-song, YAO Jun-qing, CHEN Qiang, CUI Yu, LIU Xin-wang. Effect of partial recrystallization on microstructure and tensile properties of NiFeCoCrMn high-entropy alloy [J]. Transactions of Nonferrous Metals Society of China, 2022, 32: 947−956.

[3] YANG C, KANG L M, LI X X, ZHANG W W, ZHANG D T, FU Z Q, LI Y Y, ZHANG L C, LAVERNIA E J. Bimodal titanium alloys with ultrafine lamellar eutectic structure fabricated by semi-solid sintering [J]. Acta Materialia, 2017, 132: 491−502.

[4] CAO Z H, MA Y J, CAI Y P, WANG G J, MENG X K. High strength dual-phase high entropy alloys with a tunable nanolayer thickness [J]. Scripta Materialia, 2019, 173: 149−153.

[5] ZHANG Z J, HAN X T, MA Y J, MA H, CHEN J H, LI G J, CAO Z H, WU Y C. Simultaneous enhancement in hardness and He-irradiation tolerance of TiVCr/W medium entropy nanolaminates [J]. Journal of Alloys and Compounds, 2023, 935: 168114.

[6] ZHU Cheng-yan, WU Hao, ZHU He-guo, LI Xiang-dong, TU Chun-lei, XIE Zong-han. Mechanical properties and fracture mechanism of as-cast $MnFeCoCuNi_x$ high-entropy alloys [J]. Transactions of Nonferrous Metals Society of China, 2021, 31: 222−231.

[7] CAO Z H, ZHAI G Y, MA Y J, DING L P, LI P F, LIU H L, LU H M, CAI Y P, WANG G J, MENG X K. Evolution of interfacial character and its influence on strain hardening in dual-phase high entropy alloys at nanoscale [J]. International Journal of Plasticity, 2021, 145: 103081.

[8] WANG Jian-ying, ZOU Jian-peng, YANG Hai-lin, ZHANG Li-jun, LIU Zhi-lin, DONG Xi-xi, JI Shou-xun. Exceptional strength-ductility synergy of additively manufactured

CoCrNi medium-entropy alloy achieved by lattice defects in heterogeneous microstructures [J]. Journal of Materials Science & Technology, 2022, 127: 61−70.

[9] LIAO Y C, LI T H, TSAI P H, JANG J S C, HSIEH K C, CHEN C Y, HUANG J C, WU H J, LO Y C, HUANG C W, TSAO I Y. Designing novel lightweight, high-strength and high-plasticity $Ti_x(AlCrNb)_{100-x}$ medium-entropy alloys [J]. Intermetallics, 2020, 117: 106673.

[10] LIAO Y C, YE W T, CHEN P S, TSAI P H, JANG J S C, HSIEH K C, CHEN C Y, HUANG J C, WU H J, LO Y C, HUANG C W, TSAO I Y. Effect of Al concentration on the microstructural and mechanical properties of lightweight $Ti_{60}Al_x(VCrNb)_{40-x}$ medium-entropy alloys [J]. Intermetallics, 2021, 135: 107213.

[11] YANG T, ZHAO Y L, TONG Y, JIAO Z B, WEI J, CAI J X, HAN X D, CHEN D, HU A, KAI J J, LU K, LIU Y, LIU C T. Multicomponent intermetallic nanoparticles and superb mechanical behaviors of complex alloys [J]. Science, 2018, 362: 933−937.

[12] SHIRATORI H, FUJIEDA T, YAMANAKA K, KOIZUMI Y, KUWABARA K, KATO T, CHIBA A. Relationship between the microstructure and mechanical properties of an equiatomic AlCoCrFeNi high-entropy alloy fabricated by selective electron beam melting [J]. Materials Science and Engineering A, 2016, 656: 39−46.

[13] MIRACLE D B, SENKOV O N. A critical review of high entropy alloys and related concepts [J]. Acta Materialia, 2017, 122: 448−511.

[14] CHEN Rui-run, QIN Gang, ZHENG Hui-ting, WANG Liang, SU Yan-qing, CHIU Yu-lung, DING Hong-sheng, GUO Jing-jie, FU Heng-zhi. Composition design of high entropy alloys using the valence electron concentration to balance strength and ductility [J]. Acta Materialia, 2018, 144: 129−137.

[15] TANG Zhao-wu, ZHANG Shan, CAI Rui-peng, ZHOU Qing, WANG Hai-feng. Designing high entropy alloys with dual fcc and bcc solid-solution phases: Structures and mechanical properties [J]. Metallurgical and Materials Transactions A, 2019, 50: 1888−1901.

[16] STEPANOV N D, SHAYSULTANOV D G, SALISHCHEV G A, TIKHONOVSKY M A. Structure and mechanical properties of a light-weight AlNbTiV high entropy alloy [J]. Materials Letters, 2015, 142: 153−155.

[17] HUANG Xue-jun, MIAO Jia-shi, LUO A A. Order-disorder transition and its mechanical effects in lightweight AlCrTiV high entropy alloys [J]. Scripta Materialia, 2022, 210: 114462.

[18] YURCHENKO N, PANINA E, BELYAKOV A, SALISHCHEV G, ZHEREBTSOV S, STEPANOV N. On the yield stress anomaly in a B2-ordered refractory AlNbTiVZr0.25 high-entropy alloy [J]. Materials Letters, 2022, 311.

[19] STEPANOV N D, YURCHENKO N Y, SKIBIN D V, TIKHONOVSKY M A, SALISHCHEV G A. Structure and mechanical properties of the $AlCr_xNbTiV$ (x = 0, 0.5, 1, 1.5) high entropy alloys [J]. Journal of Alloys and Compounds, 2015, 652: 266−280.

[20] SENKOV O N, SENKOVA S V, MIRACLE D B, WOODWARD C. Mechanical properties of low-density, refractory multi-principal element alloys of the Cr−Nb−Ti−V−Zr system [J]. Materials Science and Engineering A, 2013, 565: 51−62.

[21] YAN Xue-hui, LIAW P K,ZHANG Yong. Ultrastrong and ductile BCC high-entropy alloys with low-density via dislocation regulation and nanoprecipitates [J]. Journal of Materials Science & Technology, 2022, 110: 109−116.

[22] YAO Hong-wei, LIU Yong-miao, SUN Xian-hu, LU Yi-ping, WANG Tong-min, LI Ting-ju. Microstructure and mechanical properties of $Ti_3V_2NbAl_xNi_y$ low-density refractory multielement alloys [J]. Intermetallics, 2021, 133: 107187.

[23] YURCHENKO N Y, STEPANOV N D, ZHEREBTSOV S V, TIKHONOVSKY M A, SALISHCHEV G A. Structure and mechanical properties of B2 ordered refractory $AlNbTiVZr_x$ (x=0−1.5) high-entropy alloys [J]. Materials Science and Engineering A, 2017, 704: 82−90.

[24] WANG Xin-yi, MARESCA F, CAO Peng-hui. The hierarchical energy landscape of screw dislocation motion in refractory high-entropy alloys [J]. Acta Materialia, 2022, 234: 118022.

[25] WEN Xiao-can, HUANG Hai-long, WU Hong-hui, ZHOU Mei-sa, BU Ye-qiang, YUAN Xiao-yuan, JIANG Sui-he, WANG Hui, LIU Xiong-jun, WANG Hong-tao, LIU Jia-bin, WU Yuan, LU Zhao-ping. Enhanced plastic deformation capacity in hexagonal-close-packed medium entropy alloys via facilitating cross slip [J]. Journal of Materials Science & Technology, 2023, 134: 1−10.

[26] WU Zheng-gang, GAO Yan-fei, BEI H. Thermal activation mechanisms and Labusch-type strengthening analysis for a family of high-entropy and equiatomic solid-solution alloys [J]. Acta Materialia, 2016, 120: 108−119.

[27] GEORGE E P, CURTIN W A, TASAN C C. High entropy alloys: A focused review of mechanical properties and deformation mechanisms [J]. Acta Materialia, 2020, 188: 435−474.

[28] LEE Chan-ho, SONG Gian, GAO M C, FENG Rui, CHEN Pei-yong, BRECHTL J, CHEN Yan, AN Ke, GUO Wei, POPLAWSKY J D, LI Song, SAMAEI A T, CHEN Wei, HU A, CHOO H, LIAW P K. Lattice distortion in a strong and ductile refractory high-entropy alloy [J]. Acta Materialia, 2018, 160: 158−172.

[29] TODA-CARABALLO I, RIVERA-DíAZ-DEL-CASTILLO P E J. Modelling solid solution hardening in high entropy alloys [J]. Acta Materialia, 2015, 85: 14−23.

[30] CHEN Xue-fei, WANG Qi, CHENG Zhi-ying, ZHU Ming-liu, ZHOU Hao, JIANG Ping, ZHOU Ling-ling, XUE Qi-qi, YUAN Fu-ping, ZHU Jing, WU Xiao-lei, MA En. Direct observation of chemical short-range order in a medium-entropy alloy [J]. Nature, 2021, 592: 712−716.

[31] ZHANG Ruo-peng, ZHAO Shi-teng, DING Jun, CHONG Yan, JIA Tao, OPHUS C, ASTA M, RITCHIE R O, MINOR A M. Short-range order and its impact on the CrCoNi medium-entropy alloy [J]. Nature, 2020, 581: 283−287.

[32] LEI Zhi-feng, LIU Xiong-jun, WU Yuan, WANG Hui, JIANG Sui-he, WANG Shu-dao, HUI Xi-dong, WU Yi-dong, GAULT B, KONTIS P, RAABE D, GU Lin, ZHANG Qing-hua, CHEN Hou-wen, WANG Hong-tao, LIU Jia-bin, AN Ke, ZENG Qiao-shi, NIEH T G, LU Zhao-ping.

Enhanced strength and ductility in a high-entropy alloy via ordered oxygen complexes [J]. Nature, 2018, 563: 546−550.
[33] SUN Ze-rui, SHI Chang-gen, LIU Cui-xia, SHI Hang, ZHOU Jie. The effect of short-range order on mechanical properties of high entropy alloy Al0.3CoCrFeNi [J]. Materials & Design, 2022, 223: 111214.
[34] ZHAO Yang-yang, CHEN Hui-cong, LU Z P, NIEH T G. Thermal stability and coarsening of coherent particles in a precipitation-hardened $(NiCoFeCr)_{94}Ti_2Al_4$ high-entropy alloy [J]. Acta Materialia, 2018, 147: 184−194.
[35] MA Y, WANG Q, JIANG B B, LI C L, HAO J M, LI X N, DONG C, NIEH T G. Controlled formation of coherent cuboidal nanoprecipitates in body-centered cubic high-entropy alloys based on $Al_2(Ni,Co,Fe,Cr)_{14}$ compositions [J]. Acta Materialia, 2018, 147: 213−225.
[36] ARDELL A J. Precipitation hardening [J]. Metallurgical Transactions A, 1985, 16: 2131−2165.
[37] KIM W C, NA M Y, KWON H J, NA Y S, WON J W, CHANG H J, LIM K R. Designing $L2_1$-strengthened Al−Cr−Fe−Ni−Ti complex concentrated alloys for high temperature applications [J]. Acta Materialia, 2021, 211: 116890.
[38] SHI Pei-jian, ZHONG Yun-bo, LI Yi, REN Wei-li, ZHENG Tian-xiang, SHEN Zhe, YANG Bing, PENG Jian-chao, HU Peng-fei, ZHANG Yong, LIAW P K, ZHU Yun-tian. Multistage work hardening assisted by multi-type twinning in ultrafine-grained heterostructural eutectic high-entropy alloys [J]. Materials Today, 2020, 41: 62−71.
[39] MA Zi-hao, HOU Bing, QIN Dong-yang, LI Yu-long. Effect of strain rate on mechanical properties of HCP/FCC dual-phase CoCrFeNiNb0.5 high-entropy alloy [J]. Transactions of Nonferrous Metals Society of China, 2023, 33: 1144−1155.
[40] KIM J K, KIM J H, PARK H, KIM J S, YANG G, KIM R, SONG T, SUH D W, KIM J. Temperature-dependent universal dislocation structures and transition of plasticity enhancing mechanisms of the Fe40Mn40Co10Cr10 high entropy alloy [J]. International Journal of Plasticity, 2022, 148: 103148.
[41] MU Yong-kun, LIU Le, SHI Jin-qiang, SUN Tong-tong, HU Kai, JIA Yue-fei, SONG Kai-kai, JIA Yan-dong, WANG Qing, WANG Gang. Multi-type dislocation substructure evolution in a high-strength and ductile duplex high-entropy nanocomposites [J]. Composites Part B: Engineering, 2022, 247: 110322.
[42] SADEGHPOUR S, ABBASI S M, MORAKABATI M, KARJALAINEN L P. Effect of dislocation channeling and kink band formation on enhanced tensile properties of a new beta Ti alloy [J]. Journal of Alloys and Compounds, 2019, 808: 151741.
[43] MING Kai-sheng, BI Xiao-fang, WANG Jian. Realizing strength-ductility combination of coarse-grained Al0.2Co1.5CrFeNi1.5Ti0.3 alloy via nano-sized, coherent precipitates [J]. International Journal of Plasticity, 2018, 100: 177−191.
[44] YANG T, ZHAO Y L, FAN L, WEI J, LUAN J H, LIU W H, WANG C, JIAO Z B, KAI J J, LIU C T. Control of nanoscale precipitation and elimination of intermediate-temperature embrittlement in multicomponent high-entropy alloys [J]. Acta Materialia, 2020, 189: 47−59.
[45] WANG Wei-yang, ZHOU Shuang, XIAO Zhu, QIU Wen-ting, LEI Qian. Effect of aging treatment and equal channel angular pressing on microstructure evolution and properties of a CuCrZrSc alloy [J]. Journal of Alloys and Compounds, 2022, 925: 166624.
[46] ZHANG Y J, HAN D,LI X W. Impact of short range ordering on the anomalous four-stage strain hardening behavior of low solid-solution hardening Ni−Cr alloys [J]. Materials Science and Engineering A, 2021, 814: 141193.
[47] HERRMANN J, INDEN G, SAUTHOFF G. Deformation behaviour of iron-rich iron-aluminum alloys at low temperatures [J]. Acta Materialia, 2003, 51: 2847−2857.

高强度、均匀压缩塑性铸态 $Ti_x(AlVCr)_{100-x}$ 轻质中熵合金

开明杰[1]，马玉洁[2]，汪晓天[1]，程 靓[1]，胡建波[3]，胡瑶瑶[1]，徐泰然[1]，李贵江[1]，孟祥康[4]，操振华[1]

1. 南京工业大学 材料科学与工程学院，南京 210009；
2. 江苏航运职业学院 智能制造与信息学院，南通 226010；
3. 中国工程物理研究院 流体物理研究所 冲击波物理与爆轰物理重点实验室，绵阳 621900；
4. 南京大学 现代工程与应用科学学院 固体微结构国家重点实验室，南京 210093

摘 要：采用单轴压缩测试、X 射线衍射、扫描电子显微镜和透射电子显微镜等研究了 Ti 含量对铸态轻质 $Ti_x(AlVCr)_{100-x}$ 中熵合金显微组织与力学性能的影响。结果表明，随着 Ti 含量的增加，屈服强度先增加后减少。其中，$Ti_{60}(AlVCr)_{40}$ 合金的压缩强度和均匀塑性应变分别达到 1204 MPa 和 70%，并具有 255 MPa·cm^3/g 的高比屈服强度，表现出最优的综合力学性能。强化效应主要归因于固溶强化和共格纳米析出强化的协同作用，位错运动如位错钉扎、缠结及位错胞的形成能显著提高中熵合金的应变硬化能力。

关键词：TiAlVCr 中熵合金；固溶强化；*b*2 析出相；应变硬化行为

(Edited by Bing YANG)